NASA/TM-20210011828

Modeling of Electro-Magneto-Thermo-Mechanical Interactions in High-Voltage Materials and Structures for Electric Propulsion

Paria Naghipour
HX5 Sierra, LLC, Fort Walton Beach, Florida

Andrew Woodworth
Glenn Research Center, Cleveland, Ohio

Euy-Sik Shin
Universities Space Research Association, Columbia, Maryland

Maricela Lizcano
Glenn Research Center, Cleveland, Ohio

Victor Nguyen and Olesya Zhupanska
University of Arizona, Tucson, Arizona

May 2022

NASA STI Program . . . in Profile

Since its founding, NASA has been dedicated to the advancement of aeronautics and space science. The NASA Scientific and Technical Information (STI) Program plays a key part in helping NASA maintain this important role.

The NASA STI Program operates under the auspices of the Agency Chief Information Officer. It collects, organizes, provides for archiving, and disseminates NASA's STI. The NASA STI Program provides access to the NASA Technical Report Server—Registered (NTRS Reg) and NASA Technical Report Server—Public (NTRS) thus providing one of the largest collections of aeronautical and space science STI in the world. Results are published in both non-NASA channels and by NASA in the NASA STI Report Series, which includes the following report types:

- TECHNICAL PUBLICATION. Reports of completed research or a major significant phase of research that present the results of NASA programs and include extensive data or theoretical analysis. Includes compilations of significant scientific and technical data and information deemed to be of continuing reference value. NASA counter-part of peer-reviewed formal professional papers, but has less stringent limitations on manuscript length and extent of graphic presentations.

- TECHNICAL MEMORANDUM. Scientific and technical findings that are preliminary or of specialized interest, e.g., "quick-release" reports, working papers, and bibliographies that contain minimal annotation. Does not contain extensive analysis.

- CONTRACTOR REPORT. Scientific and technical findings by NASA-sponsored contractors and grantees.

- CONFERENCE PUBLICATION. Collected papers from scientific and technical conferences, symposia, seminars, or other meetings sponsored or co-sponsored by NASA.

- SPECIAL PUBLICATION. Scientific, technical, or historical information from NASA programs, projects, and missions, often concerned with subjects having substantial public interest.

- TECHNICAL TRANSLATION. English-language translations of foreign scientific and technical material pertinent to NASA's mission.

For more information about the NASA STI program, see the following:

- Access the NASA STI program home page at http://www.sti.nasa.gov

- E-mail your question to help@sti.nasa.gov

- Fax your question to the NASA STI Information Desk at 757-864-6500

- Telephone the NASA STI Information Desk at 757-864-9658

- Write to:
  NASA STI Program
  Mail Stop 148
  NASA Langley Research Center
  Hampton, VA 23681-2199

NASA/TM-20210011828

Modeling of Electro-Magneto-Thermo-Mechanical Interactions in High-Voltage Materials and Structures for Electric Propulsion

Paria Naghipour
HX5 Sierra, LLC, Fort Walton Beach, Florida

Andrew Woodworth
Glenn Research Center, Cleveland, Ohio

Euy-Sik Shin
Universities Space Research Association, Columbia, Maryland

Maricela Lizcano
Glenn Research Center, Cleveland, Ohio

Victor Nguyen and Olesya Zhupanska
University of Arizona, Tucson, Arizona

National Aeronautics and
Space Administration

Glenn Research Center
Cleveland, Ohio 44135

May 2022

This work was sponsored by the
Transformative Aeronautics Concepts Program.

Level of Review: This material has been technically reviewed by technical management.

This report is available in electronic form at http://www.sti.nasa.gov/ and http://ntrs.nasa.gov/

Modeling of Electro-Magneto-Thermo-Mechanical Interactions in High-Voltage Materials and Structures for Electric Propulsion

Paria Naghipour
HX5 Sierra, LLC
Fort Walton Beach, Florida 32548

Andrew Woodworth
National Aeronautics and Space Administration
Glenn Research Center
Cleveland, Ohio 44135

Euy-Sik Shin
Universities Space Research Association
Columbia, Maryland 21046

Maricela Lizcano
National Aeronautics and Space Administration
Glenn Research Center
Cleveland, Ohio 44135

Victor Nguyen and Olesya Zhupanska
University of Arizona
Tucson, Arizona 85721

Summary

The growing interest in developing high-voltage-, high-power-capable electrical components for electric aircraft propulsion requires a more in-depth understanding of their electrical characteristics, critical material responses, and their synergistic influence on the overall performance of the system. A model that can accurately replicate the electrical, magnetic, thermal, and mechanical operating stresses and successfully predict the performance of the components will help engineers optimize the system design for a given airframe and powertrain. The main component investigated in this study is a three-phase busbar comprising a copper conductor and layered polyimide and polytetrafluoroethylene insulation. This report presents development of a COMSOL Multiphysics® (COMSOL AB) numerical analysis model for a high-voltage busbar subjected to alternating current (AC) voltage and current loads that predicts the current density distribution and overall net current at multiple frequencies in conductors of various cross-sectional geometries. Current density distribution results were verified through comparing to available analytical solutions found in the literature to ensure model functionality and reliability. Analytical results demonstrated the influence of busbar geometry on the skin effect, phase, proximity, and current density as a function of frequency. These are key factors in designing and optimizing high-voltage AC cable systems with multiple cores, which should be taken into consideration to avoid structural failure and performance degradation. It was concluded that both the skin effect and proximity greatly depended on the geometry and the aspect ratio of a given cable system. Therefore, one should study the effect of system geometry on these phenomena before finalizing their high-voltage cable design. It is worth noting this work does not address the influence of insulation on the electromagnetic

field; rather, it is focused on the current distribution in the different conductors impacted by both transmission frequency and proximity of the conductors to each other. With the model being fully parametrized, a followup study is planned to address the insulation effects.

Nomenclature

A_{eff}	conductor cross section
AC	alternating current
r	radius of a cylindrical conductor
DC	direct current
EA	electrified aircraft
f	frequency
F-N	Fowler-Nordheim
FAA	Federal Aviation Administration
L	length of the conductor
P-F	Poole-Frenkel
PD	partial discharge
PI	polyimide
PTFE	polytetrafluoroethylene
R_{ac}	effective AC resistance
R_{dc}	DC resistance
TeDP	turboelectric distributed propulsion
μ	permeability
δ	skin depth
ρ	resistivity

Introduction

The interest in developing aircraft that reduce noise, emissions, and fuel burn has led to the research and development of electrified aircraft (EA). There are three basic categories of electrified propulsion systems being considered: all electric, hybrid electric, and turboelectric. All-electric propulsion systems store energy in batteries or use other energy-storage mechanisms, whereas turboelectric designs use turbines to drive generators, and hybrid EA depend on a combination of turbines, electric motor, and energy stored in batteries to drive propulsion. The turboelectric distributed propulsion (TeDP) concept suited toward mid- to long-range flights, including those from 1,000 miles to intercontinental, is the focus of this report. For example, a single-aisle aircraft carrying 150 passengers for intercontinental flight has two turbofan engines. Replacing each turbofan engine would require two 10-MW turboelectric fans (Refs. 1 to 3). To transmit this power across the aircraft, transmission cables or busbar systems are utilized, depending on the design. These transmission systems will experience losses measuring up to 400 kW (Ref. 4), which can lead to significant damage to the insulation. Therefore, a busbar with a reliable conductor or insulation design is necessary to operate safely under strenuous flight conditions. The transmission systems under consideration for this paper consist of alternating current (AC) power with voltages ranging from 10 to 40 kV at 500 A with a variable frequency between 400 to 4,000 Hz. These values would result in strong electric and magnetic fields that must be reduced and contained by a reliable system design. To achieve this reliable design, the electric and magnetic fields produced by the transmission must be fully analyzed and understood to help the designer optimize the system outcome.

Modeling is the most versatile tool that can be used to ensure engineering designs are safe and reliable. Models can simulate any test conditions the designer deems significant and compute the results in a matter of hours, whereas a physical test requires many more resources both financially and timewise. This report presents the development of a model that encompasses the effect of electromagnetic stresses on a given transmission system such as a busbar. Because there are many different stressors applied to the power cable system, a multilayer insulation system will most likely be needed to protect the power cable (busbar) system (Refs. 5 and 6). In current wiring systems PI/PTFE/PI, layered polyimide (PI) and polytetrafluoroethylene (PTFE), is the state-of-the-art insulation in aircraft systems. Under current industry working conditions, this multilayer insulation performed reasonably well with its good arc tracking resistance, dielectric strength, and mechanical toughness along with its high range of service temperature (Ref. 7). Therefore, the busbar system insulated with PI/PTFE/PI was considered as an initial candidate for this study and is planned to be followed by other potential candidates as the project moves forward. Because of strong electromagnetic stresses present around the busbar, developing a reliable model to analyze the high-stress areas and mitigate the conditions leading to busbar system failure is an essential step in designing busbar systems for electrified aircraft.

Catastrophic dielectric breakdown is the final failure of the electrical insulation. In this case the insulation fails, allowing an electrical arc between two parts with different electrical potentials. Examples would be between conductors in a busbar or cable, or between the conducting element and a metal structure in an aircraft such as a metal strut or tank. Catastrophic dielectric breakdown is usually preceded by degradation of the insulating properties of the insulating material. Partial discharge (PD) within the material leads to damage known as treeing. In dielectric breakdown, the potential across the dielectric is too great for the material to handle, thus allowing current to flow through the dielectric. How well a material resists the flow of this catastrophic current is represented by the material's dielectric breakdown strength. Over time, dielectric materials degrade and get weaker as they are exposed to environmental, electrical, magnetic, and thermal stresses (Ref. 5). When the material degrades, the overall dielectric strength of the system decreases from the original value, leading to premature failure. Therefore, a reliable numerical model capable of predicting this type of failure is very important throughout the design process. The PD, interpreted as dielectric breakdown (but on a microscale), occurs at high-field-stress points and/or points with lower dielectric breakdown strength. These high stress points can be created either by concentrated fields that emerge from the design of components (e.g., bends, connectors, etc., in a distribution system) or from where pockets of air or foreign material are introduced in the component material via manufacturing or processing. These defects tend to have significantly lower breakdown strength than the surrounding insulating material. Therefore, operating within the rated voltage range can lead to PD and avoid a complete dielectric breakdown (Ref. 8). The second condition in which PD occurs is when the electric field is stronger in certain areas of the insulation than the rest. These areas of magnified electric potential result from electron trapping and space charge (Ref. 9). A special case of PD is corona: when the electric field outside the insulation is high enough to break down the medium outside of the insulation (Ref. 10). The main consequence of PD is that it deteriorates the insulation material. When a burst of energy is released in the form of current on the inside of the insulation, damage is caused by the energy dissipated and charged ions that are produced (Ref. 11). This causes the defect to grow slightly because of chemical or mechanical breakdown occurring in the material. Electrons will then repeat a new cycle of trapping around that defect, now larger, and once enough charge is accumulated PD will occur again, and the cycle continues. The defect will continue growing, branching, and spreading across the material in a tree-like pattern. This treeing is one of the most critical forms of electrical degradation (Ref. 5). Once the tree has grown large enough, a significant drop in dielectric breakdown strength of the insulating material can be observed. The size and rate in which the treeing spreads varies

depending on certain conditions of the energy source and the insulation material properties. The rate at which PD cycles occur, the size of the tree expected to grow, and the effects the treeing has on the overall dielectric strength need to be considered to predict the electrical system's life (Ref. 9).

A model based on fundamental science needs to be developed that will accurately replicate real test results. Five commonly accepted and widely used models studying degradation in transmission systems are briefly presented and discussed here. It will be necessary to understand what conditions will trigger one phenomenon over another or if there will be multiple failure mechanisms taking place.

One of the most comprehensive studies on aging of aircraft wiring insulations was performed by Joseph Kurek in 2008 titled "Aircraft Wiring Degradation Study" (Ref. 12). In this study, there were 32 sets (setups) of samples, each having 11 specimens. Twenty-six of the setups experienced aging under various conditions. All of the wire samples were 22-gauge (0.025-in. diameter) nickel-coated copper conductor wrapped with two layers of fluorocarbon-coated PI film and a PTFE outer wrap. The samples were loaded with 1,500 V_{ac} at 60 Hz during the time-dependent dielectric breakdown, keeping the applied electrical loads constant over time. A result of this extensive study, sponsored by the Federal Aviation Administration, is that oxidation and humidity have little to no effect on the performance of the system, whereas thermal and mechanical stresses have great effect on the life of the insulating ability of this system (Refs. 12 and 13). The above-mentioned study (Ref. 12) covers a wide range of variables, with multiple variables being simultaneously changed, making it difficult to pinpoint one specific mechanism responsible for system degradation and failure. Therefore, dielectric breakdown models addressing individual mechanisms leading to system failure are more helpful in understanding and improving a system's design (Ref. 14):

(1) The first model of interest widely used in literature is the E-model. The E-model is based on a thermochemical theory and includes bond breakage as the mechanism leading to electrical insulation failure. McPherson and Mogul (Ref. 15) explain that both covalent and ionic forces need to be considered to estimate bond strength, or else the model will underpredict breakage strength. The advantage of this approach is that it already includes thermal stresses in the electric model. The important properties that need to be considered when adapting this model to a high-voltage application is the difference in activation energy (enthalpy) and the material's acceleration parameter γ (Ref. 15). This acceleration parameter predicts how fast the bonds will continue to break once there is enough energy to initiate the degradation.

(2) The second model of interest is the 1/E model, which is a current-based model where current flows through the dielectric via Fowler-Nordheim (F-N) conduction (Ref. 15). The emissions of electrons are induced by an electrostatic field, and electron movement within the lattice damages the dielectric because of impact ionization (Refs. 16 and 17). That is, electron trapping leads to the buildup of a local current density, causing local failure. Unlike the E-model, the 1/E model does not account for temperature effects, which is a main disadvantage for current-based models.

(3) Similar to the 1/E model, the third model of interest is the $\sqrt{E}$-model, the basis of which is the current leakage flowing through the dielectric. For high-quality dielectrics, the dominant current flow is always through F-N conduction, whereas for lower quality dielectrics, the conduction mechanism may be Poole-Frenkel (P-F) or Schottky conduction (Refs. 16 to 18). This is the primary difference in the two models (1/E and $\sqrt{E}$) and their equations. Like any of the current-based models, the $\sqrt{E}$ model fails to explain the temperature dependence and why the activation energy reduces strongly with field. Also note that in the $\sqrt{E}$ model with P-F conduction, the bond breakage energy is grossly overpredicted, leading to a nonconservative design.

(4) The fourth model is the power model (Refs. 19 and 20), based on the breakdown of the hydrogen bonds in a given dielectric medium, which leads to failure. The hydrogen interacts with the lattice and

breaks additional weak bonds within the material, which then leads to forming a percolation path that will allow current to pass, resulting in dielectric breakdown. Hydrogen bonds usually get into the interface of the materials because of hydrogen-based processing methods. Therefore, if the dielectric in a given busbar system is manufactured and processed in a way where unwanted hydrogen is not introduced in the lattice, this model and failure mechanism may not be of concern.

(5) The last model (E^2-model) describes ionic injection as the failure mechanism in dielectrics. Metal injection and electron transport together cause this phenomenon (Ref. 21). Copper oxidation at the conductor surface produces copper ions that penetrate the insulation. The ions move around in the lattice much like an electron would, but the effects are greater because the ion is larger. The ions also act as a percolation path (Ref. 21). If there are enough ions within the lattice, current can pass through and lead to dielectric breakdown. Because an EA application must be highly reliable, a high-quality manufacturing process should be used that reduces surface oxidization so it is not an issue. The behavior of the model will also be dependent on the conductor material, which may not necessarily be pure copper.

From the models discussed above, two are based on bond breaking, one is based on the movement of ions, and two are based on electron trapping. The models based on the breakdown of bonds are crucial because they include temperature dependence and can be carried over to high-power insulation, such as high-voltage busbar designs. The thermal-electric analysis can be applied to observe the behavior of polymer chains. The chains can stretch, break, or move, which would cause defects or even high-stress areas within the busbar and the insulating material. The models based on ion movement are another valuable tool in assessing system durability. The ionic movement resulting from the large electric potential in high-voltage busbar designs might weaken the bonds at specific spots within the polymer chain (Refs. 21 and 22) and consequently reduce overall strength. The electron-trapping models, presenting a clear understanding of how degradation occurs over time, are also of importance. Electron trapping results in a local area accumulating a net charge, which then leads to PD to release the energy. This PD in turn leads to the growth of the defected area, treeing out of the defect, and eventually reduction in the dielectric breakdown strength of the insulation, causing failure. Another important aspect of electron trapping is the breaking of polymer chains. The kinetic energy of mobile electrons in the material can be enough to break the polymer chain. As the temperature of the insulating material increases, the amount of energy necessary to break a polymer chain decreases. Therefore, the likelihood of an electron having enough energy to break a weakened polymer chain significantly increases. These concepts signify the importance of tracking and predicting electron behavior. Understanding how the material properties and input power conditions affect the electrons' behavior is an essential step in constructing accurate numerical models.

Overall, different failure mechanisms can play a significant role in causing dielectric breakdown. Each model presents important physical and chemical reactions that result from movement of electrons. Understanding how temperature and mechanical stresses affect these defects, interfaces, and boundaries within a cable system will lead to a better understanding of the influence these stressors have on electron movement and how the system degrades and fails over time. Research on developing mathematical models to understand electron movement/behavior is plentiful (Refs. 15 to 22). However, there has not been much emphasis in available literature on how a given system geometry can influence these failure mechanisms. There is a recent study to specifically address the influence of system geometry on the failure of multilayer insulation systems for electrified propulsion (Ref. 23); however, the number of available studies in this context still remains low. Frequency, skin effect, phase, and the proximity and/or geometry of the conductors are the key factors in designing and optimizing high-voltage AC cable systems with multiple conductors. Therefore, the main objective of this work is to develop an in-house finite element model that can help engineers gain a better understanding of how these key factors are

affected by varying the cable geometry, and how the geometry can be modified and optimized to reach the desired performance. After this Introduction, the finite element model of the multicore cable system is described in detail, followed by results and discussions and a brief conclusion.

Finite Element Model

This work investigates the electromagnetic phenomena in a three-phase busbar system consisting of the copper conductor and PI/PTFE/PI insulation system shown in Figure 1. The AC load on the busbar is expected to be up to 500 A and 40 kV and have a frequency range between 400 and 4,000 Hz.

For comparison purposes and to gain experience and understanding of the electromagnetic phenomena, simpler configurations—a single-phase busbar system and equivalent square and circular configurations—are also analyzed (Figure 2). Analysis of these configurations constitutes an important step in the development of models for the three-phase busbar system. The circular configuration is useful as there are several closed-form solutions developed for this geometry, serving as a first-step verification tool for the numerical model. The single-phase busbar configuration allows the effects of the rectangular geometry and aspect ratio to be explored prior to moving to the more complicated three-phase busbar system.

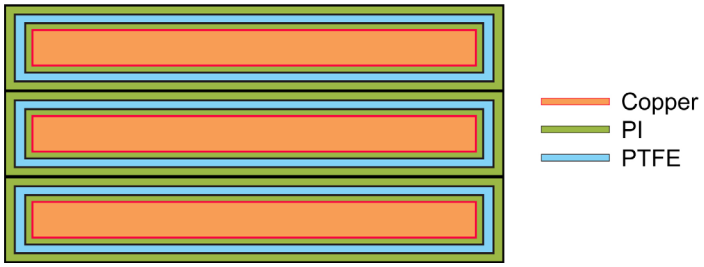

Figure 1.—Three-phase busbar system: copper core conductor is wrapped in three-layer insulation consisting of polyimide (PI) and polytetrafluoroethylene (PTFE).

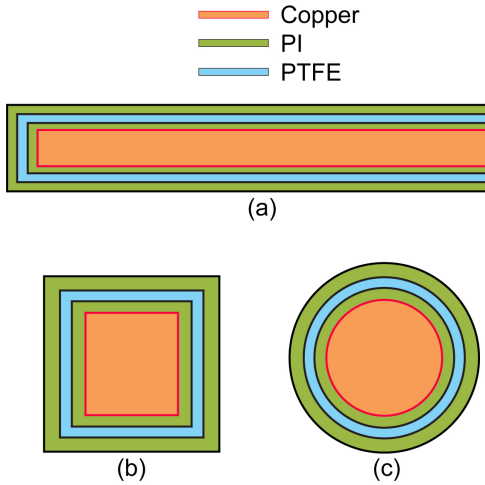

Figure 2.—Single-phase busbar configurations. (a) Rectangular. (b) Square. (c) Circular.

The dimensions of the single busbar in the model are as follows: The copper core is 76.2 by 3.175 mm, the thickness of the PI/PTFE layers is 0.5 mm, and the thickness of each PTFE layer is 0.4 mm; this leads to a dielectric strength of 197 to 272 kV/mm. When rectangular, square, and circular configurations are simulated, the cross-sectional area of the copper conductor and the thickness of the insulations are kept the same as that of the busbar system. A perfect bonding among the insulation layers is assumed in all cases. The single-phase system maintains the same dimensions as a single bar in the three-phase busbar system. Table I lists model geometries used in the present study.

The boundary conditions include current or voltage (up to 20 kV amplitude, frequency range 0 to 5,000 kHz) applied at one end of the copper core. Voltage is also specified at the conductor/insulator interface (i.e., copper core/PTFE layer boundary). Since the effect on the fields of air is insignificant compared to on the insulation and because corona generation is not considered at this time, creating an air volume around the system was not included. Since this is a model for an aircraft transmission system, no ground was assumed in preliminary designs. Figure 3 illustrates how boundary conditions are applied.

Properties of the materials used in this study are listed in Table II (Refs. 24 to 26). Computational studies have been performed using COMSOL Multiphysics® finite element analysis software (Ref. 27).

TABLE I.—SINGLE-PHASE BUSBAR MODEL GEOMETRIES

Conductor cross-sectional geometry	Height, mm	Width, mm	Area, mm^2
Rectangular	3.175	76.2	241.935
Square	15.55	15.554	241.803
Circular	8.776 (radius)	----------	241.960

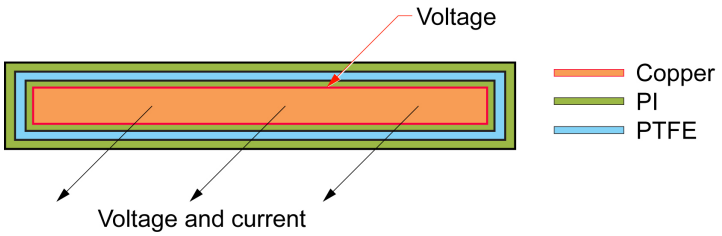

Figure 3.—Boundary conditions for busbar model (40 kV_{ac}).

TABLE II.—BUSBAR MATERIAL PROPERTIES

Material	Electrical resistivity, Ω	Relative permittivity	Relative permeability
Copper	1.68×10^{-8}	6.0	0.999991
Polyimide	1×10^{17}	2.1[a]	1
PTFE	1.5×10^{17}	3.4[b] 3.5[c]	1

[a]Independent of frequency and temperature.
[b]At 25 μm and 1 kHz.
[c]At 100 μm and 1 kHz.

Results and Discussion

Skin Effects

Skin effect is a phenomenon that occurs in AC transmission systems where electrical current migrates towards the surfaces of the conductor. The "skin" of the current density is the distance δ from the surface where the current density has dropped to ~0.37 of the maximum current density. A system experiencing skin effect shows a large gradient of current density throughout the conductor cross section, where the current migrates towards the surface of the conductor. The magnitude of the phenomenon is a function of the AC frequency and the resistivity ρ of the conducting material. Unlike direct current (DC) systems that are carrying electrons in one direction, AC systems have cyclical loading where the current is flowing alternately in both directions. Skin effect is the result of a frequency-dependent phase difference between the electric and magnetic fields inside of the conductor. The phase difference forces the current towards the surface of the conductor, therefore reducing the current density in the center. As the net current flow is maintained, the edges of the conductor experience a higher current density than that of the center. As the frequency increases, the skin depth decreases. With this decrease in skin depth, the current density in the skin is higher, creating an effective smaller conductor cross section A_{eff} carrying the current. Reduced effective cross-sectional area increases the resistance. The measure of this effect was termed the "effective resistance," R_{ac}. It is as if a fluid (current) were being pushed through only a small opening (skin effect) after part of the tubing was blocked. As frequency f increases, the effective resistance also increases. This needs to be considered when predicting the power losses and heat generated in the transmission systems carrying AC currents.

To investigate the significance of skin depth, the circular configuration is studied first. The following discussion presents illustrations of computational results for the three-phase circular configuration that can be verified through available closed-form solutions in literature (Ref. 6). Initial results reveal a promising trend in matching available solutions reported by Corcoran and Nagy (Ref. 6), whose closed-form analytical model showed the skin depth calculated as

$$\delta = \sqrt{\frac{\rho}{\pi f \mu}} \tag{1}$$

and the effective AC resistance as

$$R_{ac} = \frac{\rho L}{A_{eff}} = \frac{R_{dc}}{A_{eff}} \tag{2}$$

where μ is the permeability, L is the length of the conductor, R_{dc} is the DC resistance, and

$$A_{eff} = \delta\pi(2r - \delta) \tag{3}$$

for the conductor of radius r (see Table I).

Figure 4 shows the current density variation across the circular cross section when a constant AC current was applied at different frequencies. The blue line represents 0 Hz (DC) and shows a uniform current density throughout the core. The yellow line represents 5,000 Hz, which shows that most of the current is bunched up against the outside of the conductor and therefore has the highest current density and the smallest skin depth. It is seen that as the frequency increases, the skin depth decreases. To compensate for the reduction in the skin depth, the current density in the active arc of the conductor starts rising. It is important to note that at high enough frequencies, there is a region that has current flowing in the opposite direction, which is sometimes referred to as the "negative current."

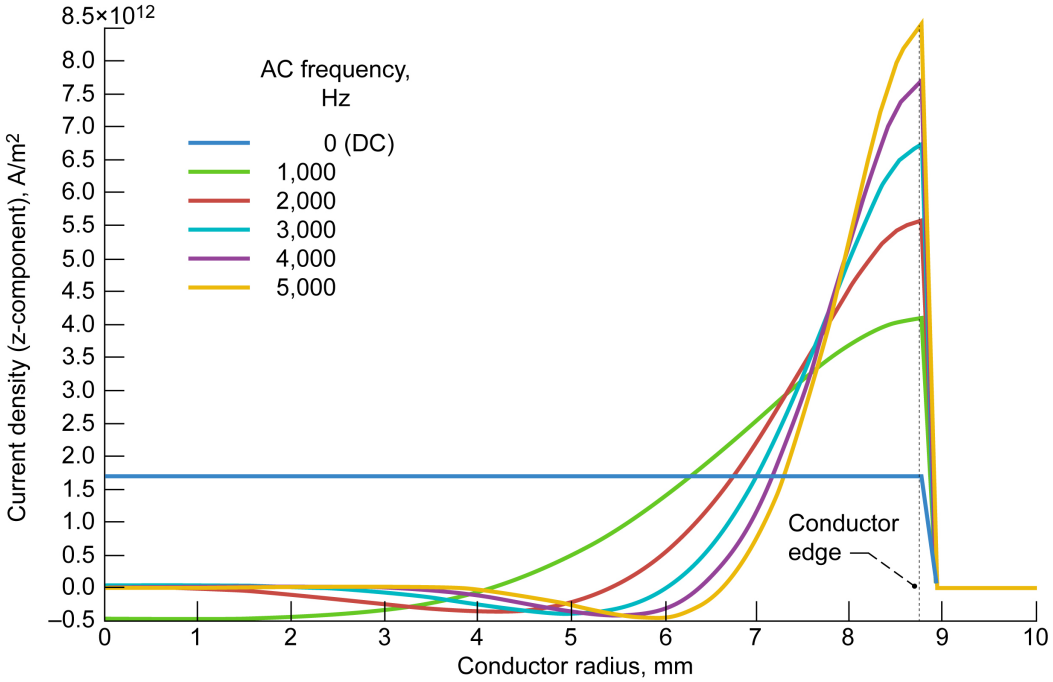

Figure 4.—Current density versus radius at constant alternating current (AC) load of various frequencies for busbar with circular cross section. DC is direct current.

The skin effect increases the effective resistance of the conductor. Based on the Ohm's law ($V = IR$), if the resistance R increases, the voltage V must also increase to maintain the same net current I. If the voltage remains constant, the net current will decrease. The effects of skin depth (changing current density) on the electromagnetic profile of a cable or busbar need to be considered when evaluating the performance of a particular design. This calls for investigation of the current density behavior in the cable under constant voltage. Figure 5 shows the current density variation across the circular cross section when a constant AC voltage was applied at different frequencies. The line representing 0 Hz (i.e., DC constant voltage) shows a constant current density throughout the core. The line representing 5,000 Hz shows the highest current density value and the smallest skin depth. It is shown that there is a significant difference in the current density profiles between the constant-voltage and the constant-current cases. Unlike the DC loading, the AC loadings show a distinct peak and sharp drop in the current density curve at the skin depth region. In the case of the AC constant current, peaks in the current density distributions are below the DC value, whereas they are above the DC value for the constant-voltage case.

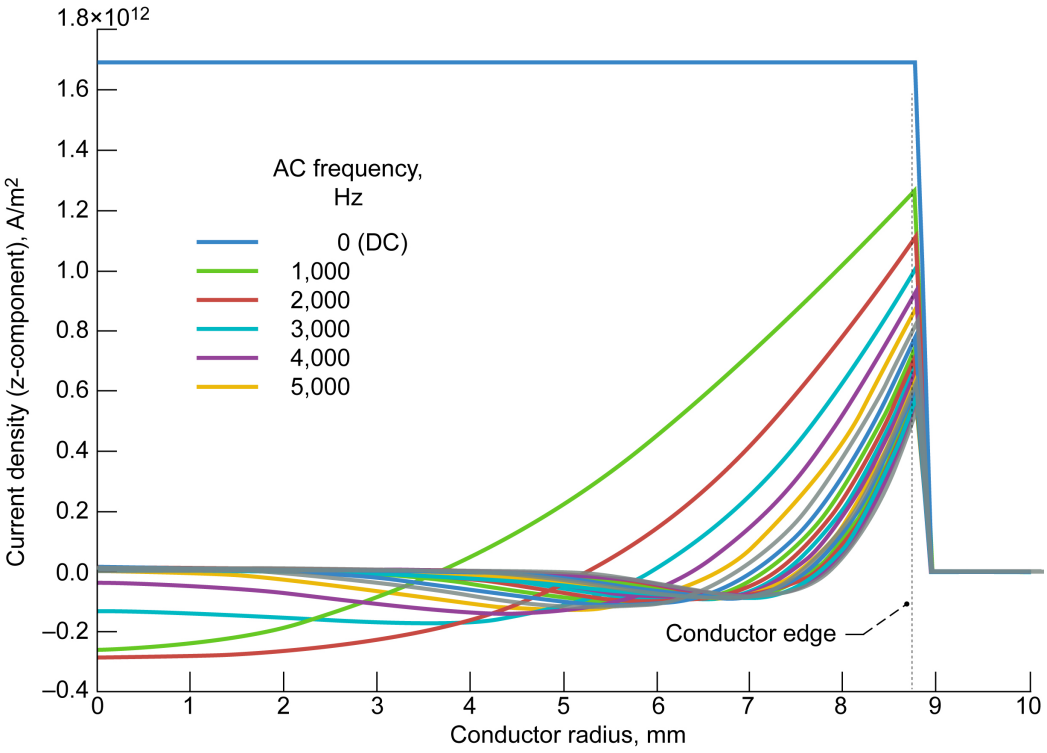

Figure 5.—Current density versus radius at constant alternating current (AC) voltage load of various frequencies for busbar with circular cross section. DC is direct current.

Table III summarizes calculation results of the skin depth in the copper circular conductor subjected to the AC constant-voltage load with frequencies ranging from 60 to 5,000 Hz. Figure 6 shows comparisons in the skin depth calculated using the above equations and from the model for the circular cross section (constant-voltage source, 4,000 Hz). Results from the finite element model are found to be in very good agreement with the analytical results.

TABLE III.—CLOSED-FORM MODEL RESULTS OF SKIN DEPTH IN CIRCULAR COPPER CONDUCTOR SUBJECTED TO CONSTANT ALTERNATING CURRENT (AC) VOLTAGE

Frequency, Hz	Skin depth, mm
60	8.42
400	3.26
1,000	2.06
2,000	1.46
3,000	1.19
4,000	1.03
5,000	0.92

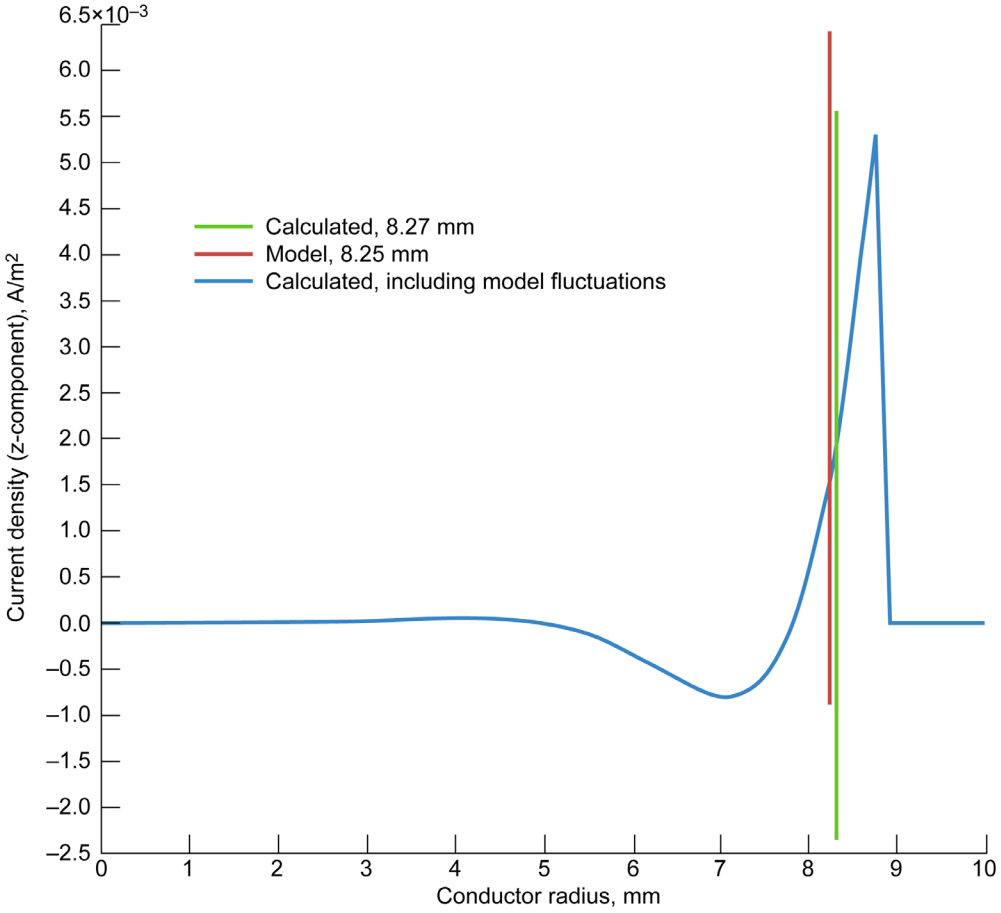

Figure 6.—Comparison of skin depth calculated with closed-form equations of Reference 6 and COMSOL Multiphysics® (COMSOL AB) model for busbar with circular cross section (constant-voltage source, 4,000 Hz frequency).

Figure 7 shows the effective resistance versus frequency, and Figure 8 shows the net current versus frequency calculated for a round copper wire of 250 Ω (1.47×10^{10} m long). Results from computational studies as well as those obtained using analytical models (Refs. 6 and 28) are shown. The agreement between analytical and numerical results confirms the reliability of the model.

To explore the effect of geometry on the skin effects, the equivalent square and rectangular (single busbar shown in Figure 2) configurations were analyzed. The overall cross-sectional areas of the copper conductors for both configurations are equal to that of the circular conductor. The thicknesses of the corresponding insulation layers were kept the same as well. The same boundary conditions were used for all configurations studied. Figure 9 shows contour plots of the current density in the circular, square, and rectangular cross-sectional configurations, respectively. Please note that for the sake of simplifying and accelerating the computation, the rectangular busbar model exploits the vertical axis of symmetry (cutting the modeled busbar in half left to right). Therefore, only the right half of the busbar is modeled as the other half is identical. This common modeling technique is applicable when the geometry, material properties, and boundary conditions are all symmetrical across the chosen axis of symmetry.

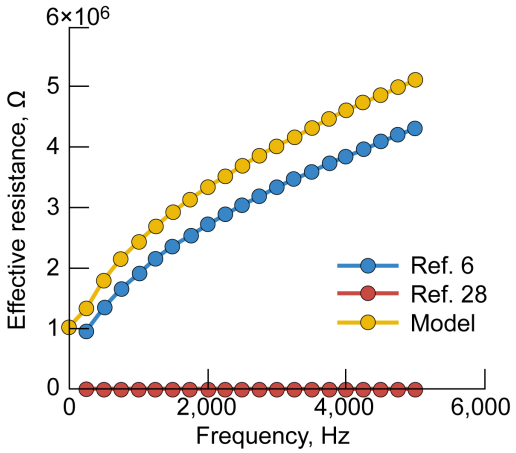

Figure 7.—Comparison of calculated and COMSOL Multiphysics® (COMSOL AB) model results for effective resistance versus frequency of copper conductor with circular cross section.

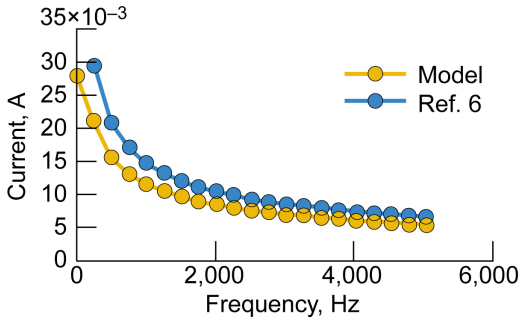

Figure 8.—Comparison of calculated and COMSOL Multiphysics® (COMSOL AB) model results for current versus frequency of copper conductor with circular cross section.

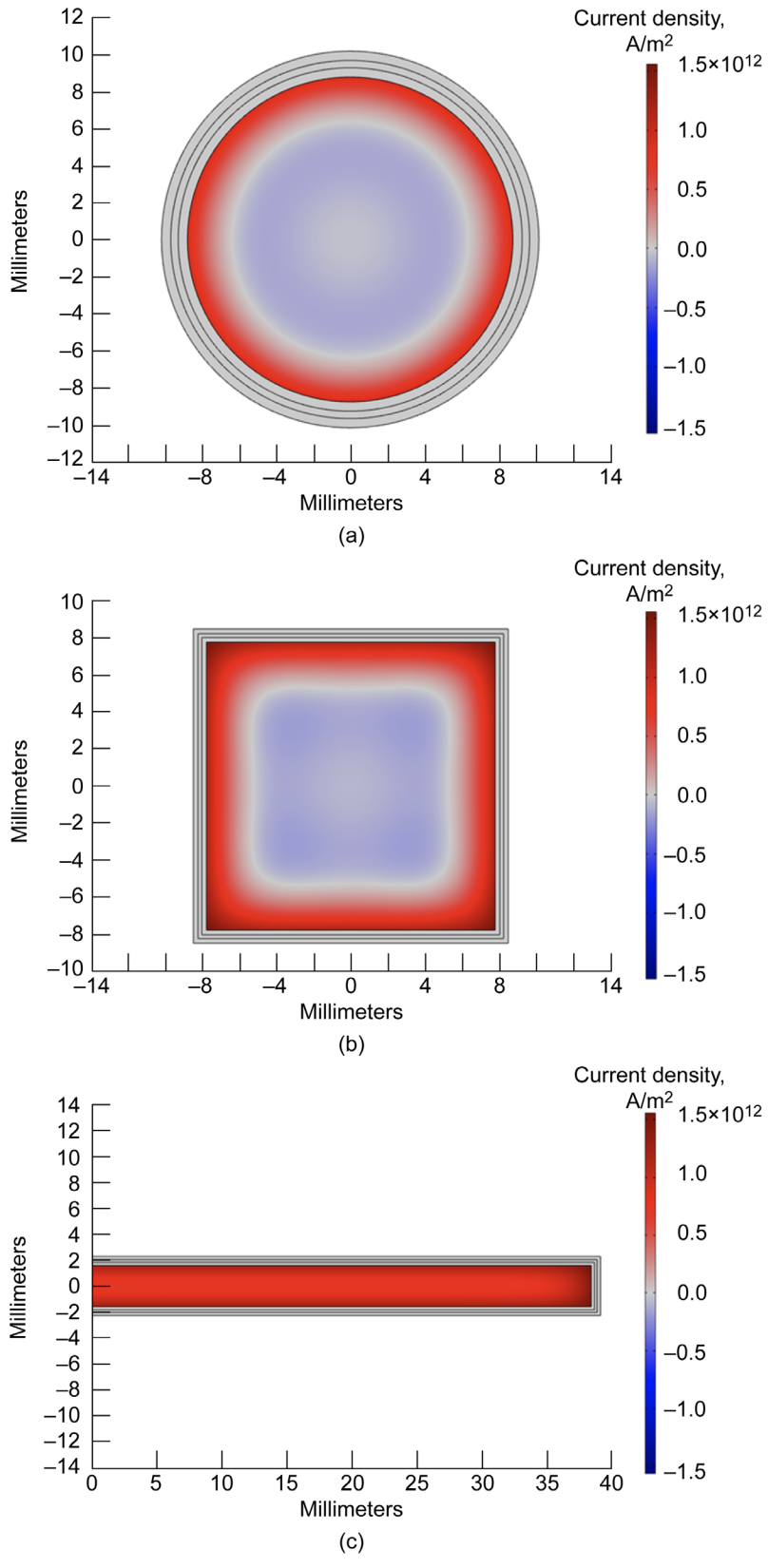

Figure 9.—Current density distribution at 1,000 Hz of busbars of different cross sections with constant-voltage source. (a) Circular. (b) Square. (c) Rectangular.

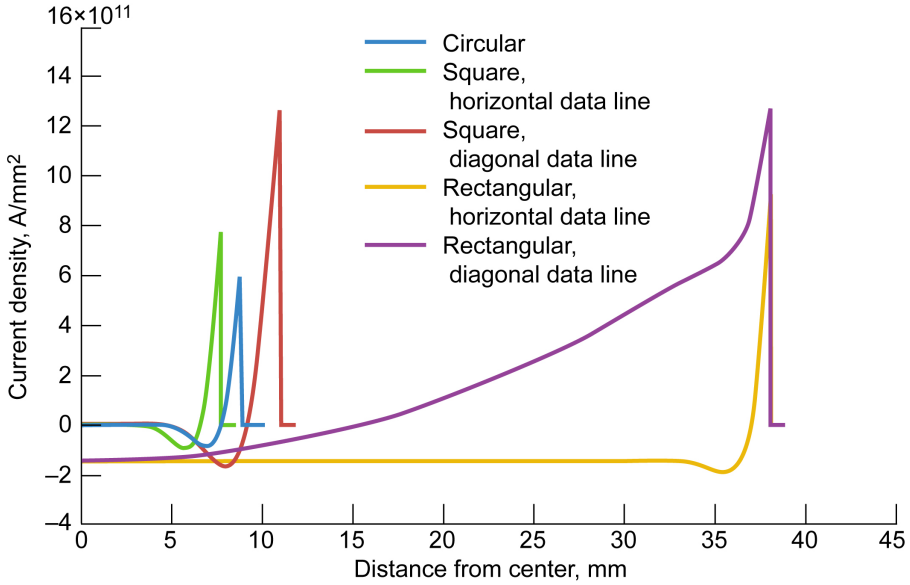

Figure 10.—Comparison of current density for different busbar configurations with constant-voltage source.

The current density is seen to be higher in the rectangular busbar than in other configurations. Figure 10 compares the current density as a function of distance from center among the circular, square, and rectangular cross sections.

As visible in Figure 10, the maximum current density of similar magnitude was formed at the corners in the square and rectangular cases. Also note that an increase in the rectangular aspect ratio leads to an increase in the reported maximum current density. It is worth mentioning that horizontal profiles generate the typically reported current density plot. Comparing the square and rectangular cross sections, their peak values were similar along the diagonal data line regardless of the considered profile. The horizontal data line current density shows a higher peak value for the rectangular geometry because the midpoint of the rectangle right-hand edge is much closer to the corner (where the peak current density is) than the midpoint of the square right-hand edge. Although both square and rectangular cross sections show some negative conduction along their respective horizontal profiles, the rectangular geometry maintains a much greater area under the curve with positive current density, indicating a larger overall current. Distributions of the current density in the rectangular busbar along different profiles are shown in Figure 11.

Figure 12 shows net current versus frequency in the circular, square, and rectangular cross sections given a constant-voltage source. It is seen that the net current increases with an increase in the aspect ratio of the busbar, where the horizontal busbar with narrow rectangular cross section carries the highest current (most significantly in the 500 to 3,000 Hz range). Below 3,000 Hz the rectangular busbar carries more than 2 times more current, with a maximum of ~7 times more at 500 Hz. As the skin depth approaches half of the copper conductor thickness, a conductively underutilized region starts developing in the center of the conductor. Because the aspect ratios of the circular and square conductors are much smaller, their underutilized areas develop at lower frequencies. The underutilized areas are visually apparent in Figure 9(a) and Figure 9(b).

Figure 13 shows a contour plot of the current density distribution for the busbar of the rectangular cross section at 1,000 Hz. The busbar seems to have very minimal negative current. This contour plot can be used as an input for a hierarchical thermal model, where thermal fields are estimated based on a given current density profile in a busbar.

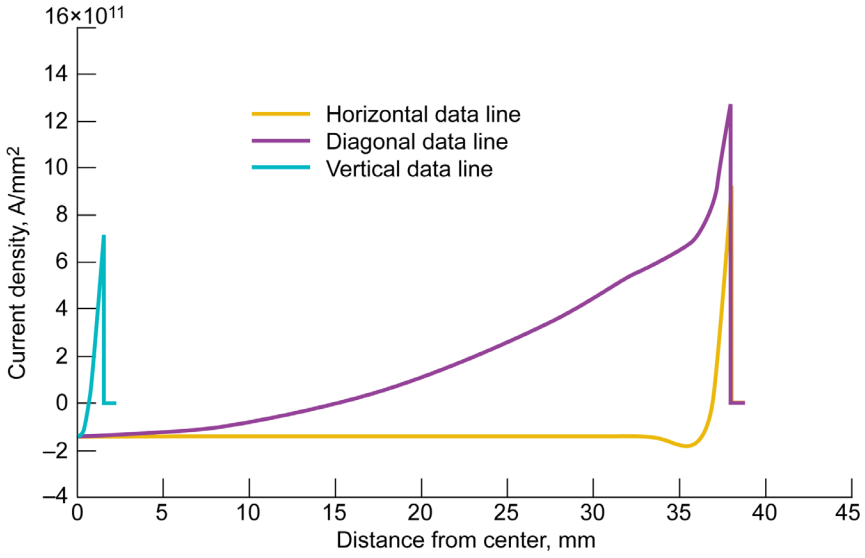

Figure 11.—Current density distribution of rectangular busbar configuration with constant-voltage source.

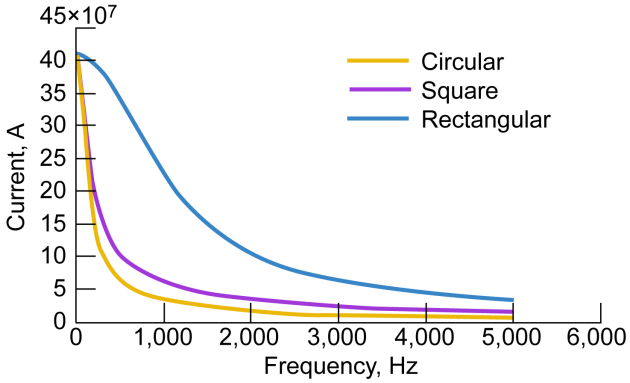

Figure 12.—Net current versus frequency for busbars of different configurations.

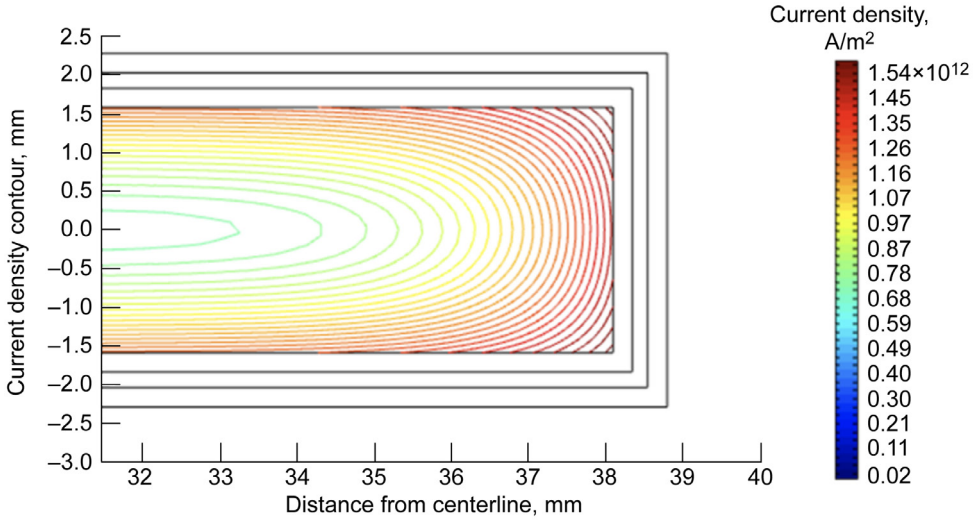

Figure 13.—Current density contours for rectangular busbar configuration with constant-voltage source at 1,000 Hz.

Phase and Proximity Effects

After addressing the skin effects, proximity and the influence of relative phase are addressed in this section. Proximity effect is where electromagnetic fields in adjacent conductors influence electrical current densities in each other. Electromagnetic fields are influenced by both the magnitude of current flow and direction. Geometrical considerations such as distance between conductors and relative positioning have a great impact on how conductors affect one another's electromagnetic fields. Stacked circular and square cross section configurations analyzed in this section clearly show that both the proximity and skin effect take place simultaneously in the system. In most industry applications, cables are grouped up in threes, and the cores (i.e., AC) are arranged in a three-phase system, where the loads are separated by one-third of a cycle (offset by 120° from one another). Figure 14 illustrates a three-phase square configuration and shows the current density distribution in the bottom square at 4,000 Hz. Proximity effect is clearly demonstrated: the current density distribution is not symmetric with different peaks near the top and bottom of the square. If the proximity effect were not taking place, the current density distribution would be symmetric across the square.

Similarly, Figure 15(a) shows the three-phase circular cross section configuration, and Figure 15(b) shows the corresponding current density distribution. The proximity effect resulted in the highest current density peaks from the outside conductors (Figure 15(b)). The middle conductor was affected the least since both peaks were identical within numerical tolerance.

When comparing the proximity effect between the circular and square stacks, the square stack appears to have a more significant proximity effect since the peak values of the current density have a greater difference from one another in the square system (Figure 14 vs. Figure 15).

It was also observed from the initial analysis that the proximity effect depends significantly on the relative phase of the conductor rather than the physical position of the conductor. Figure 16 shows a snapshot of the cable cross section at three different points in the 360° cycle. Figure 17 shows net current versus frequency for the left, middle, and right orientations, respectively, shown in Figure 16; and Figure 18 demonstrates the relationship between the proximity effect and the distance at 1,000 MHz. The two conductors indicated by the arrows in Figure 18 are in the same phase, as can be seen by the same overall behavior (a red center and a blue edge). The conductor in the middle of the stack is affected more significantly by the proximity effect, with a distinct blue lip on the bottom surface of the conductor. The floating bar does not have this trait. Based on the results shown in Figure 16 to Figure 18, the behavior of the conductor depends more on the relative phase rather than its position in the stack. For example, the conductor with the 120° offset behaves the same whether it is positioned at the bottom, in the middle, or at the top. The current density profiles and the net current in that conductor do change slightly because of the position and distance from the other conductors, but the overall behavior remains unchanged.

Figure 19 shows the impact on net current due to proximity and skin effects in a rectangular busbar system. The arrangement of phases is the same as the one for the square stack shown in Figure 16. As expected, the proximity effect shows similar trends for both the rectangular and square busbars; however, the rectangular geometry tends to carry more net current than the square geometry at nonaerodynamic frequencies.

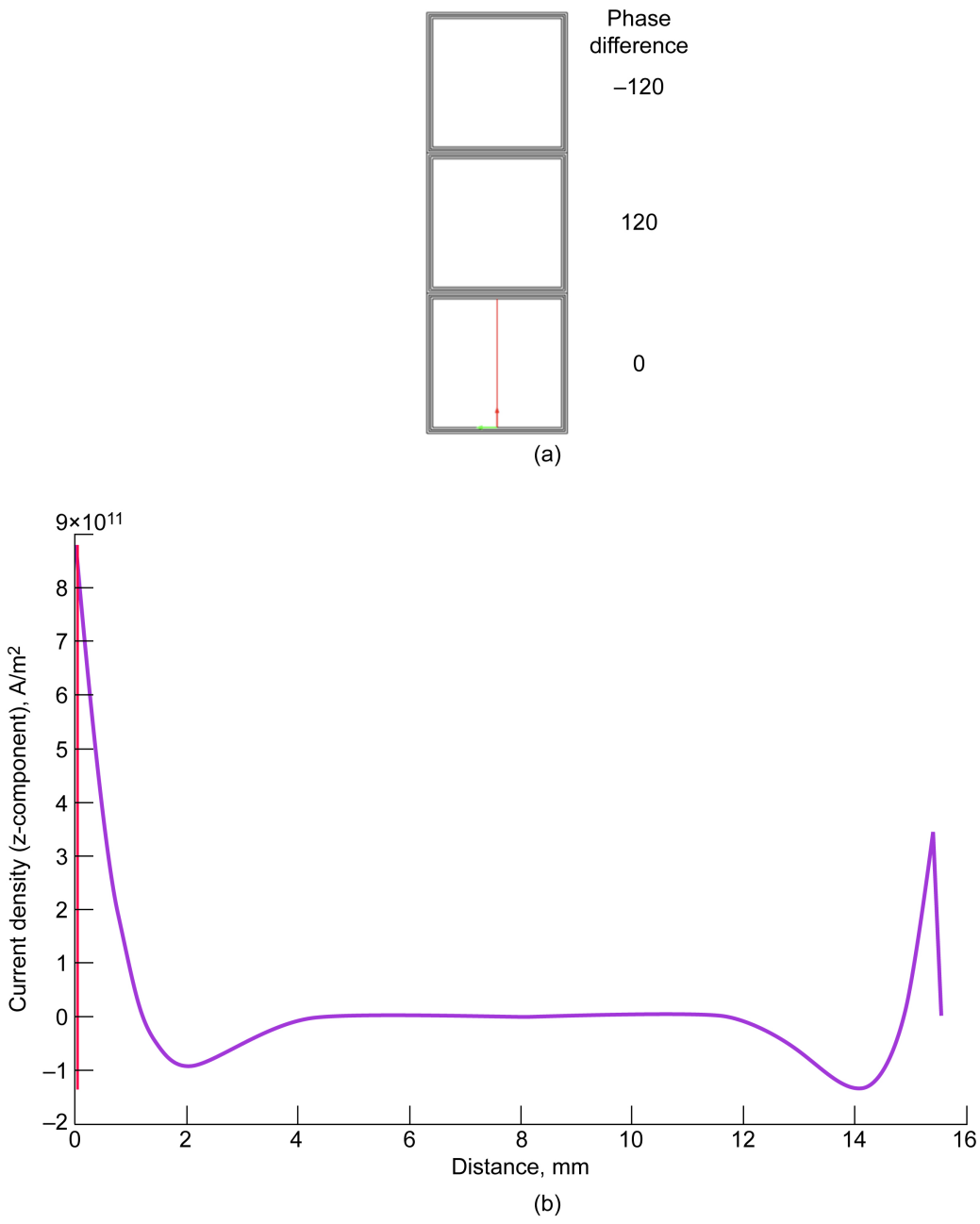

Figure 14.—Three-phase square configuration of busbar. (a) Illustration of phase difference. (b) Current density distribution along data line, where 0 is bottom edge and 0.16 m is adjacent to center square.

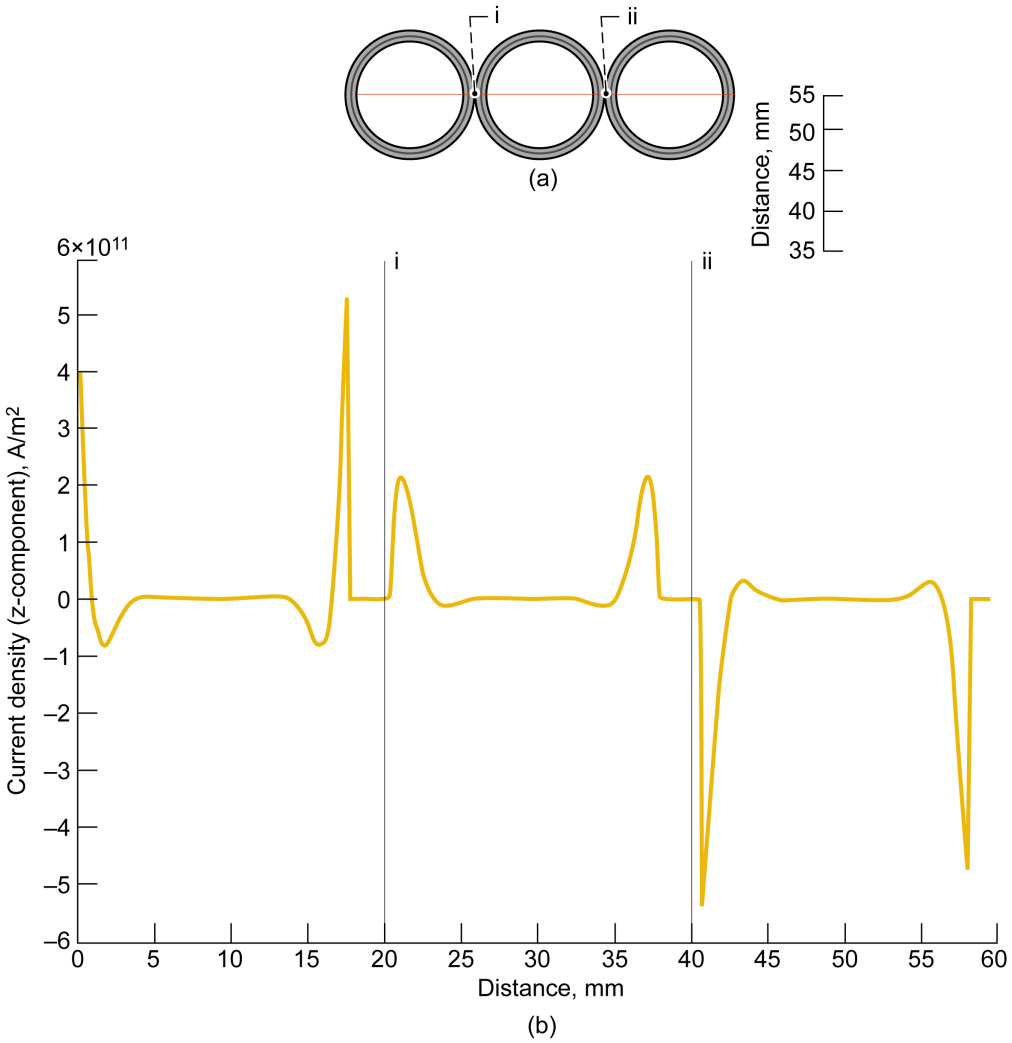

Figure 15.—Three-phase circular configuration of busbar. (a) Showing data line depicted by red line. (b) Current density distribution across data line; frequency is 4,000 Hz.

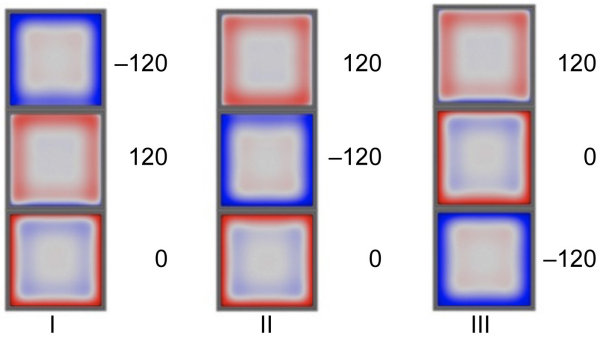

Figure 16.—Effect of phase orientation and stacking sequence on current density distribution of busbar with square configuration.

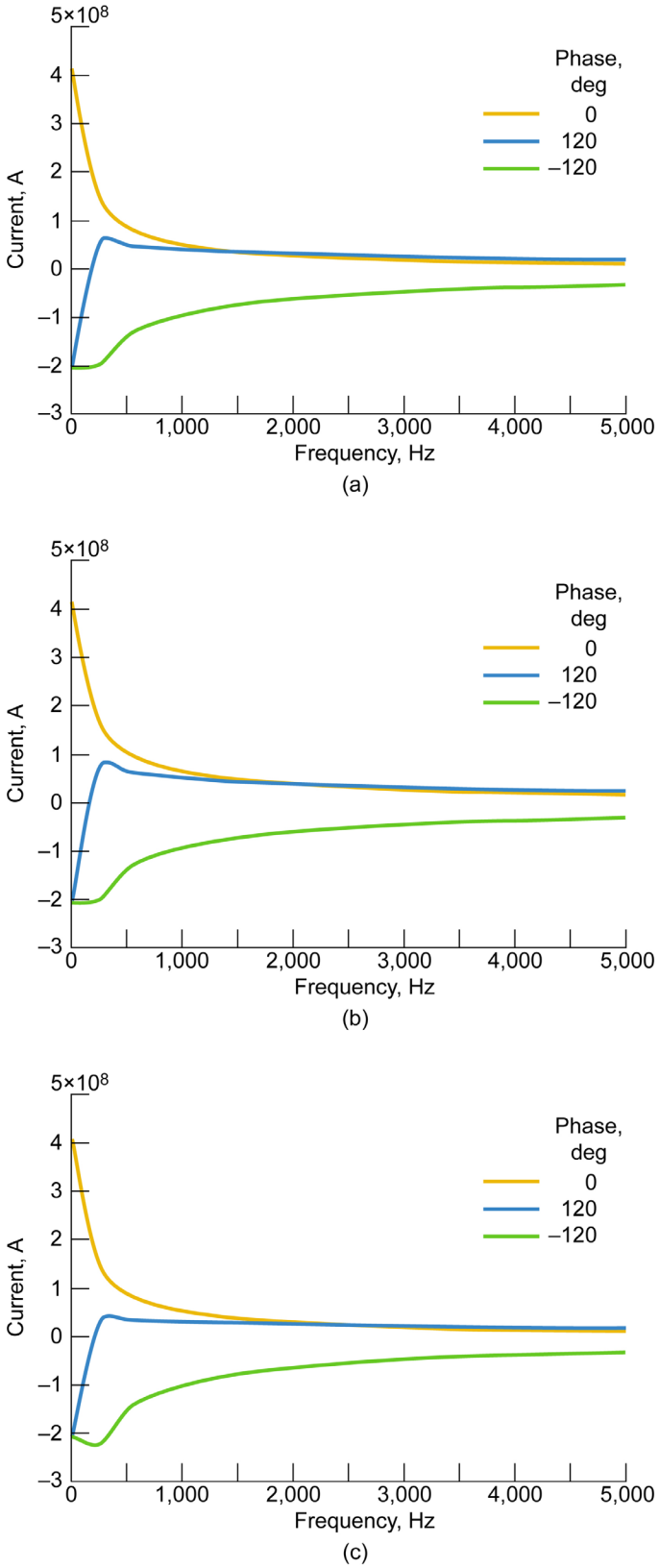

Figure 17.—Net current versus frequency for phase orientations of busbar with square configuration shown in Figure 16. (a) I. (b) II. (c) III.

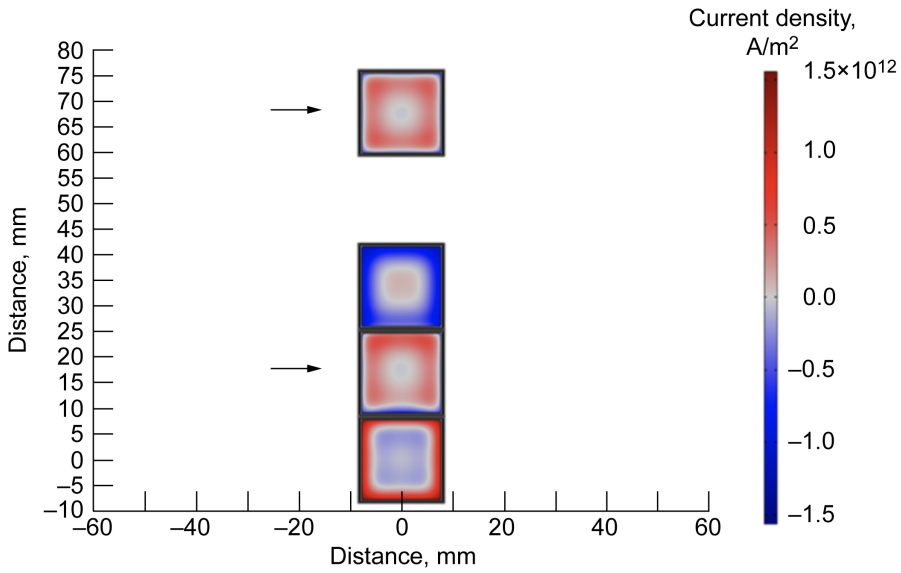

Figure 18.—Proximity effect versus distance at 1,000 Hz for busbars with square configuration.

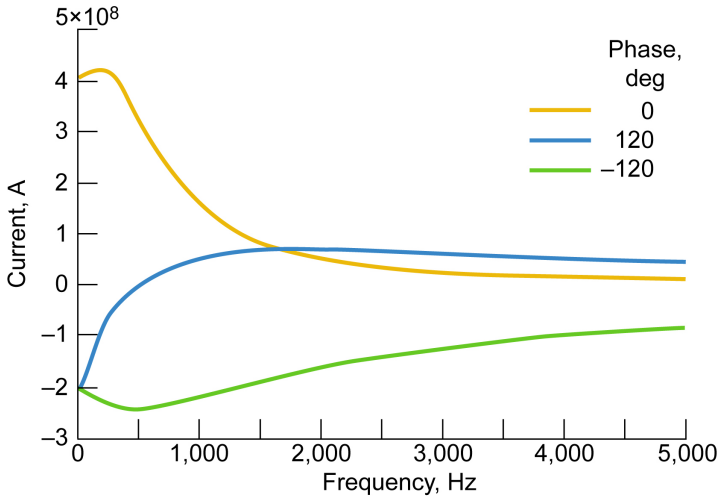

Figure 19.—Net current versus frequency for three-phase busbar with rectangular configuration.

Concluding Remarks

The modeling of busbars presented here primarily focused on how the current distribution in the different conductors was impacted by both transmission frequency and proximity of the conductors to each other. The current distribution (time-varying charge distribution) will impact the joule heating and the external field distribution, both of which are expected to be impacted by the insulation. Therefore, although this modeling work does not show how the electromagnetic fields would be impacted by choice of insulation, it shall be considered as an initial summary of the completed modeling work and serve as a guidance package for the planned followup study addressing the insulation effect.

A three-phase busbar comprising a copper conductor and insulation of layered polyimide (PI) and polytetrafluoroethylene (PTFE), PI/PTFE/PI, was modeled with the COMSOL Multiphysics® (COMSOL AB) finite element package to achieve a better understanding of the system's electromagnetic response

under alternating current (AC) load (up to 500 A, 40 kV, and a frequency of 400 to 4,000 Hz). To ensure model functionality and reliability, results were verified through available analytical solutions in literature. It was observed that both the skin and proximity effects greatly depended on the geometry and the rectangular aspect ratio of a given busbar system, which will consequently have an influence on the current density distribution as a function of frequency. These are key factors in designing and optimizing high-voltage AC cable systems with multiple cores, and therefore, one should study the effect of cable system geometry on these phenomena before finalizing their high-voltage cable design.

This numerical work needs to be elaborated further to include mechanisms such as dielectric breakdown of insulations and a thermal component, which will be addressed in our future work. Since the numerical model is well parametrized, the authors also plan to perform some parametric studies on the multilayer insulation system to investigate the effects of

- Individual layer thickness, number of layers, and material composition on dielectric breakdown voltage or partial discharge potentials
- Surrounding medium on insulation performance
- Current type on insulation performance

References

1. Jansen, Ralph, et. al.: Sizing Power Components of an Electrically Driven Tail Cone Thruster and a Range Extender. AIAA 2016–3766, 2016.
2. Dever, Timothy P., et. al.: Assessment of Technologies for Noncryogenic Hybrid Electric Propulsion. NASA/TP—2015-216588, 2015. https://ntrs.nasa.gov
3. Felder, James; Tong, Michael; and Chu, Julio: Sensitivity of Mission Energy Consumption to Turboelectric Distributed Propulsion Design Assumptions on the N3–X Hybrid Wing Body Aircraft. AIAA 2012–3701, 2012.
4. Jankovsky, Amy; Bowman, Cheryl; and Jansen, Ralph: Building Blocks for Transport-Class Hybrid and Turboelectric Vehicles. 2016. https://ntrs.nasa.gov/api/citations/20170006238/downloads/20170006238.pdf Accessed Aug. 31, 2021.
5. Malik, N.H.; Al-Arainy, A.A.; and Qureshi, M.I.: Electrical Insulation in Power Systems. CRC Press, Boca Raton, FL, 1998.
6. Corcoran, J.; and Nagy, P.B.: Compensation of the Skin Effect in Low-Frequency Potential Drop Measurements. J. Nondestruct. Eval., vol. 35, no. 58, 2016.
7. IPC Task Group: Requirements and Acceptance for Cable and Wire Harness Assemblies. IPC/WHMA–A–620D, 2020.
8. Berger, L.I.: Dielectric Strength of Insulating Materials. http://chemistry.mdma.ch/hiveboard/rhodium/pdf/chemical-data/diel_strength.pdf Accessed Aug. 31, 2021.
9. Wang, Yani, et. al.: Effect of Temperature on Space Charge Detrapping and Periodic Grounded DC Tree in Cross-Linked Polyethylene. IEEE Trans. Dielectr. Electr. Insul., vol. 23, no. 6, 2016, pp. 3704–3711.
10. Vas, J.V.; and Thomas, M.J.: Surface Degradation of Silicone Rubber Nanocomposites Due to DC Corona Discharge. IEEE Trans. Dielectr. Electr. Insul., vol. 21, no. 3, 2014, pp. 1175–1182.
11. Morshuis, P.H.F.: Degradation of Solid Dielectrics Due to Internal Partial Discharge: Some Thoughts on Progress Made and Where You Go Now. IEEE Trans. Dielectr. Electr. Insul., vol. 12, no. 5, 2005, pp. 905–913.

12. Kurek, Joseph: Aircraft Wiring Degradation Study: The PTFE/Polyimide Composite Aging and Test Results. DOT/FAA/AR–082, 2008.
13. Ellion, D.K.: A Standardized Procedure for Evaluating the Relative Thermal Life and Temperature Rating of Thin-Wall Airframe Wire Insulation. IEEE Trans. Dielectr. Electr. Insul., vol. EI–7, no. 1, 1972, pp. 16–25.
14. Krevelen, D.W.; and Nijenhuis, K.: Properties of Polymers: Their Correlation With Chemical Structure; Their Numerical Estimation and Prediction From Additive Group Contributions. Elsevier, Amsterdam, 2009.
15. McPherson, J.W.; and Mogul, H.C.: Underlying Physics of the Thermochemical E Model in Describing Low-Field Time-Dependent Dielectric Breakdown in SiO_2 Thin Films. J. Appl. Phys., vol. 84, no. 3, 1998.
16. McPherson, J.W.: Time Dependent Dielectric Breakdown Physics—Models Revisited. Microelectron. Reliab., vol. 52, nos. 9–10, 2012, pp. 1753–1760.
17. Chen, Ih-Chin; Holland, S.E.; and Hu, Chenming: Electrical Breakdown in Thin Gate and Tunneling Oxides. IEEE Trans. Electron Devices, vol. 32, no. 2, 1985, pp. 413–422.
18. Allers, K.-H.: Prediction of Dielectric Reliability From I–V Characteristics: Poole-Frenkel Conduction Mechanism Leading to Root E Model for Silicon Nitride MIM Capacitor. Microelectron. Reliab., vol. 44, no. 3, 2004, pp. 411–423.
19. Sune, J.; and Wu, E.Y.: Hydrogen-Release Mechanisms in the Breakdown of Thin SiO_2 Films. Phys. Rev. Lett., vol. 92, no. 8, 2004, p. 087601.
20. McPherson, J.W.: On Why Dielectric Breakdown Strength Reduced With Dielectric Thickness. Presented at the 2016 IEEE International Reliability Physics Symposium, Pasadena, CA, 2016.
21. Achanta, R.; and McLaughlin, P.: A Charge Transport Based Acceleration Model for Interlevel Dielectric Breakdown. Presented at the 2011 Reliability Physics Symposium, Monterey, CA, 2011.
22. Borja, Juan Pablo; Lu, Toh-Ming; and Plawsky, Joel: Dielectric Breakdown in Gigascale Electronics: Time Dependent Failure Mechanisms. SpringerBriefs in Materials, 2016.
23. Wei, Zhuo, et al.: Partial Discharge Inception Characteristics of Twisted Pairs Under Single Voltage Pulses Generated by Silicon-Carbide Devices. IEEE Trans. Transp. Electrification, 2021.
24. DuPont Kapton: Summary of Properties. https://www.dupont.com/content/dam/dupont/amer/us/en/products/ei-transformation/documents/EI-10142-Kapton-Summary-of-Properties.pdf Accessed Sept. 2, 2021.
25. Dupont: Teflon PTFE. http://www.rjchase.com/ptfe_handbook.pdf Accessed Sept. 2, 2021.
26. WS Hampshire Inc.: PolyTetraFluoroEthylene. http://catalog.wshampshire.com/Asset/psg_teflon_ptfe.pdf Accessed Sept. 2, 2021.
27. COMSOL: Multiphysics Finite Element Analysis Software. https://www.comsol.com/ Accessed May 24, 2022.
28. Shin, Euy-Sik Eugene: Development of High Voltage Micro-Multilayer Multifunctional Electrical Insulation (MMEI) System. AIAA 2019–4511, 2019.